Available online at www.sciencedirect.com

SciVerse ScienceDirect

Geochimica et Cosmochimica Acta 95 (2012) 213–226

Geochimica et Cosmochimica Acta

www.elsevier.com/locate/gca

# Nano-scale investigation of the association of microbial nitrogen residues with iron (hydr)oxides in a forest soil O-horizon

Marco Keiluweit [a,b], Jeremy J. Bougoure [b], Lydia H. Zeglin [a], David D. Myrold [a], Peter K. Weber [b], Jennifer Pett-Ridge [b], Markus Kleber [a], Peter S. Nico [c,*]

[a] *Department of Crop and Soil Science, Soil Science Division, Oregon State University, Corvallis, OR, USA*
[b] *Chemical Sciences Division, Physical and Life Sciences Directorate, Lawrence Livermore Laboratory, Livermore, CA, USA*
[c] *Earth Sciences Division, Lawrence Berkeley National Laboratory, Berkeley, CA, USA*

Received 10 October 2011; accepted in revised form 1 July 2012; available online 22 July 2012

---

**Abstract**

Amino sugars in fungal cell walls (such as chitin) represent an important source of nitrogen (N) in many forest soil ecosystems. Despite the importance of this material in soil nitrogen cycling, comparatively little is known about abiotic and biotic controls on and the timescale of its turnover. Part of the reason for this lack of information is the inaccessibility of these materials to classic bulk extraction methods. To address this issue, we used advanced visualization tools to examine transformation pathways of chitin-rich fungal cell wall residues as they interact with microorganisms, soil organic matter and mineral surfaces. Our goal was to document initial micro-scale dynamics of the incorporation of $^{13}$C- and $^{15}$N-labeled chitin into fungi-dominated microenvironments in O-horizons of old-growth forest soils. At the end of a 3-week incubation experiment, high-resolution secondary ion mass spectrometry imaging of hyphae-associated soil microstructures revealed a preferential association of $^{15}$N with Fe-rich particles. Synchrotron-based scanning transmission X-ray spectromicroscopy (STXM/NEXAFS) of the same samples showed that thin organic coatings on these soil microstructures are enriched in aliphatic C and amide N on Fe (hydr)oxides, suggesting a concentration of microbial lipids and proteins on these surfaces. A possible explanation for the results of our micro-scale investigation of chemical and spatial patterns is that amide N from chitinous fungal cell walls was assimilated by hyphae-associated bacteria, resynthesized into proteinaceous amide N, and subsequently concentrated onto Fe (hydr)oxide surfaces. If confirmed in other soil ecosystems, such rapid association of microbial N with hydroxylated Fe oxide surfaces may have important implications for mechanistic models of microbial cycling of C and N.

© 2012 Elsevier Ltd. All rights reserved.

---

## 1. INTRODUCTION

Structurally complex microbial amino sugars are an important component of carbon (C) and nitrogen (N) cycling in soil ecosystems. High microbial demand and strong competition for easily assimilable C and N compounds in these systems may promote the development of adaptive features to better utilize amino sugar C and N. Amino sugars are derived predominantly from cell wall components of bacteria and fungi (Guggenberger et al., 1999; Amelung et al., 2001a,b). For example, chitin and its monomeric building block N-acetyl-glucosamine (NAG) comprise a significant pool of organic N in many soils (Stevenson, 1982; Amelung, 2003) and appear to be utilized by microbial communities in N-poor soils (Olander and Vitousek, 2000; Zeglin et al., 2012). Despite their importance as an organic N source in N-limited ecosystems, little is known about possible abiotic and biotic controls on the microbial utilization of N in fungal cell wall components.

---

* Corresponding author. Address: Earth Sciences Division, Lawrence Berkeley National Laboratory, 1 Cyclotron Rd., Berkeley, CA 94720, USA. Tel.: +1 510 486 7118; fax: +1 510 486 5686.
*E-mail address:* PSNico@lbl.gov (P.S. Nico).

0016-7037/$ - see front matter © 2012 Elsevier Ltd. All rights reserved.
http://dx.doi.org/10.1016/j.gca.2012.07.001

In order to exploit decomposing fungal hyphae as an N source, microorganisms produce the enzyme NAGase (commonly called chitinase), which depolymerizes the cell wall polymer chitin into monomeric subunits (i.e., NAG) that can be assimilated (Sinsabaugh et al., 1993). Elevated respiration and N mineralization rates as well as higher NAGase activity potentials in soils with high fungal biomass (so-called ectomycorrhizal mats) highlight the ability of microorganisms in such microenvironments to rapidly cycle C and N (Griffiths et al., 1990; Kluber et al., 2010). High NAGase activity may thus reflect a high microbial demand for amino sugars and/or a high abundance of microbiota that can utilize this N-source. In recent incubation experiments, Zeglin et al. (2012) showed that microbial communities associated with ectomycorrhizal mat patches assimilate amino sugar N more efficiently than microbial communities present in non-mat O-horizon soil. These observations strongly support the notion that microbial communities (predominantly bacteria) associated with mycorrhizal mats efficiently utilize amino sugar substrates in this microenvironment.

To date, only circumstantial evidence exists for a possible role of abiotic controls in amino sugar turnover. However, several independent observations suggest a role of the mineral matrix in amino sugar cycling. Amino sugars can adsorb to both crystalline mineral phases such as kaolinite and goethite (Kaiser and Zech, 2000) and to the hydroxylated surfaces of poorly crystalline metal (hydr)oxides such as ferrihydrite (Mikutta et al., 2010). Other sources suggest that the mere presence of minerals does not alter the rate of amino sugar turnover but rather the relative proportions of N assimilated by bacteria and fungi (Amelung et al., 2001a,b). So while there is reason to infer a role of abiotic processes in amino sugar cycling, the precise mechanisms involved remain obscure. Furthermore, although the general affinity of carbohydrates for Fe oxides is well-documented (Kiem and Koegel-Knabner, 2002, 2003; Eusterhues et al., 2011), neither the time scale of formation of such associations nor their ecological importance N-limited systems has been well investigated.

Understanding the micro-scale complexity present in heterogeneous soil systems poses significant challenges for conventional bulk methods. To characterize soil microstructures associated with fungal hyphae and to identify and trace amino sugars from fungal cell wall components and its transformation products into the soil microenvironment, we employed a novel combination of isotopic and spectroscopic imaging techniques. First, synchrotron-based scanning transmission X-ray microscopy (STXM) in combination with near-edge X-ray absorption fine structure (NEXAFS) spectroscopy, which has been employed to interrogate structurally intact soil micro-aggregates (Wan et al., 2007; Lehmann et al., 2005; Kinyangi et al., 2006), offers chemically sensitive spectroscopic imaging of biological and environmental samples with high spatial resolution (<30 nm). Second, high-resolution mass spectrometry imaging with a Cameca NanoSIMS 50 has previously been used to track specific isotopes of organic compounds in natural (Herrmann et al., 2007) and artificial soil microstructures (Müller et al., 2012) with better than 100 nm resolution.

Our conceptual approach was to take advantage of the synergistic effects of NanoSIMS and STXM/NEXAFS imaging. Applied to the same sample, NanoSIMS allowed us to follow isotopically-labeled amino sugars from fungal cell walls as they became metabolized or bound to minerals and SOM, while with STXM/NEXAFS spectromicroscopy we could determine the chemical transformations of C and N functionalities of this substrate during the process. The general goal was to visualize the fate of $^{13}$C- and $^{15}$N-labeled fungal cell wall material and determine the effects and relative importance of the microbial drivers and abiotic controls of the initial dynamics on initial amino sugar breakdown in soils. The specific objectives of this study were to (i) determine the short-term fate of fungal cell wall material in hyphal-associated microenvironments and (ii) identify potential abiotic factors such as attachment to mineral surfaces or native SOM that might affect microbial N cycling. In this microenvironment, we expected amino sugar cycling to be rapid and micron-scale imaging methods to be particularly suited to probe for the location and chemistry of the labeled fungal cell wall material and its transformation products. We focused our analyses on the interface between fungal hyphae (the natural source of chitin-rich cell wall materials) and the adjacent soil matrix containing abundant microorganisms, SOM, and minerals.

## 2. MATERIALS AND METHODS

### 2.1. Sample characteristics

#### 2.1.1. Soil characteristics

For this experiment $^{13}$C- and $^{15}$N-labeled fungal cell wall material was incubated for 3 weeks with O-horizon soil collected under Douglas-fir in the H.J. Andrews Experimental Forest (Oregon, USA). The O-horizons sampled for this experiment are characterized by abundant patches of ectomycorrhizal mats. Fungal hyphae in these mat-colonized organic soils can constitute up to 50% of dry weight (Ingham et al., 1991) and may serve as a natural source of chitinous cell wall material. The underlying soils are coarse loamy mixed mesic Typic Hapludands according to US taxonomy (Soil Survey Staff, 2010), and have a mean O-horizon depth of 6 cm. O-horizon samples had a pH of 4.5–4.8, and an organic matter content of 638 ± 22 mg/g dry mass (mean ± SE) (Zeglin et al., 2012) as determined by loss-on-ignition (Nelson and Sommers, 1996). Thus, while clearly dominated by organic matter, the O-horizon material contains a significant proportion of mineral constituents.

#### 2.1.2. Soil incubations

To obtain $^{15}$N- and $^{13}$C-labeled fungal cell wall material, Baker's yeast (*Saccharomyces cerevisiae*) was cultured in media containing 99 atm% $^{13}$C-glucose and 99 atm% $^{15}NH_4^+$ (Cambridge Isotope Laboratories, USA). After harvest, cells were washed and chemically treated to isolate insoluble chitin-enriched cell wall material (Roff et al., 1994; Kirchman and Clarke, 1999). In brief, cells were bead-beaten to break cell walls and release cytoplasmic molecules, washed, treated with 4% sodium dodecyl sulfate at 90 °C for 2 h before and after incubation with proteinase K overnight, bead-beaten and washed again, and extracted twice with a 1:1 mixture of chloroform:methanol; this protocol was designed to preferentially remove water- and organic-soluble cell debris and cell wall glycoproteins. Finally, because insoluble *S. cerevisiae* cell wall polymers are dominated by glucans (Cabib and Bowers, 1971; Watson et al., 2009), the material was incubated with 1–3-glucanase overnight at 37 °C, thus enriching the material in chitin. The molar C:N ratio of the resulting material was 20:1, implying a 2:1 ratio of glucan (6C) to amino sugar (8C:1N) molecules in the final polymeric material, and the amino sugar content of the material was independently estimated at 39% using analyses described in Zeglin et al. (2012).

The $^{15}N$ and $^{13}C$ enrichment of the cell wall material were determined using a LECO (St. Joseph, MI, USA) isotope ratio mass spectrometer (IRMS) at the Oregon State University Stable Isotope Research Unit, and were referenced to $N_2$ in air and Vienna Pee Dee Belemnite (VPDB), respectively. Multiple batches of cell wall material combined and had average $\delta^{15}N$ values of 501‰ and $\delta^{13}C$ values of 151‰. For the soil incubation, 1% w/w (dry mass basis) of suspended fungal cell wall material was mixed in 10 g dry (approximately 30 g wet at field water holding capacity) soil in airtight 500 mL Ball Jars as described in Zeglin et al. (2012). Incubations were maintained for 3 weeks at 24 °C in the dark, after which whole soil was sampled for STXM/NEXAFS and NanoSIMS analysis. After the incubation, subsamples were also collected to determine the isotopic enrichment of the bulk soil and chloroform-extracted microbial biomass using IRMS.

### *2.1.3. Specimen preparation*

To allow for high-resolution SIMS imaging and STXM/NEXAFS spectromicroscopic analysis of the same sample specimen, the samples were required to have limited topography and the ability to withstand high vacuum. They also had to be dry, conductive, and thin enough to allow photon transmission (<1 μm) and prepared without carbon-based reagents. The preparation described in the following was found to consistently isolate fungal hyphae, including associated soil bacteria and minerals, from the soil. After the incubation, the soil was thoroughly mixed and three subsamples of approximately 400 mg of soil were gently dispersed in 2 ml of 10 mM NaCl for 1 min. Larger soil particles were allowed to settle for 15 min and the individual supernatants were removed. For each subsample, 1 μL of the supernatant (containing numerous hyphal fragments) was dried on silicon nitride ($Si_3N_4$) windows (Silson Ltd., England). Samples were sputter-coated with 5 nm of iridium and then mapped using scanning electron microscopy (SEM) on a JEOL 7401 SEM (Tokyo, Japan) at Lawrence Livermore National Laboratory, CA (LLNL) with an accelerating voltage of 1 kV. Regions of interest (ROIs) for SIMS and STXM imaging analyses were selected based on morphology (i.e., targeting microstructures that included fungal hyphae, bacteria and minerals) and sample thickness.

## **2.2. Synchrotron-based scanning transmission X-ray microscopy (STXM) in combination with near edge X-ray absorption fine structure (NEXAFS) spectroscopy**

### *2.2.1. Imaging analysis*

STXM analysis of six ROIs identified by SEM was performed on the Molecular Environmental Sciences beamlines 5.3.2.2 (250–600 eV) and 11.0.2 (80–2000 eV) (Kilcoyne et al., 2003; Warwick et al., 2003) of the Advanced Light Source (ALS) at Lawrence Berkeley National Laboratories. These X-ray microscopes use a Fresnel zone plate lens to focus a monochromatic X-ray beam onto the sample. Imaging contrast relies on core electron excitation by absorption of soft X-ray radiation (Kirz et al., 1995). The sample is scanned through the fixed beam and transmitted photons are detected via a scintillator–photomultiplier detector assembly to provide 2D images of the sample volume probed.

STXM/NEXAFS at the bend magnet beamline 5.3.2.2 was used to perform C and N spectromicroscopy. The energy was calibrated at the C 1s edge using the 3p Rydberg peak of gaseous $CO_2$ at 292.74 and 294.96 eV (Ma et al., 1991) and at the N 1s edge using the 1s–$\pi^*$ transition of $N_2$ at 401.10 eV (Sodhi and Brion, 1984). Dwell times for the collection of C and N NEXAFS stacks were $\leqslant$1.2 ms to avoid potential beam damage. No visible alteration of the spectra was observed under these conditions. The spatial and spectral resolution during our measurements was 40–50 nm and ~0.1 eV, respectively. Clean areas of the $Si_3N_4$ membrane were used to normalize the transmission signal obtained from analyzed regions of interest. After recording of C and N NEXAFS stacks, Fe 2p absorption spectra were collected using small slit sizes to limit the incident flux at the undulator beamline 11.0.2. Dwell time, step size as well as the spatial and spectral resolution for Fe NEXAFS scans was as described for C and N NEXAFS.

Transmission images at energies below and at the relevant absorption edge energies were converted into optical density (OD) images [$OD = \ln(I_0/I)$, with $I_0$ being the incident photon flux and $I$ the transmitted flux]. Image sequences (also called "stacks") acquired at multiple energies spanning the relevant absorption edge (278–330 eV for C 1s edge, 390–440 eV for N 1s edge, and 690–740 eV for Fe 2p edges) were used to extract NEXAFS spectra.

Standard spectra were collected from pure reference compounds (i.e., N-acetyl-glucosamine, sodium alginate, and bovine serum albumin) in powder form. The standard materials were finely ground with an agate mortar, suspended in filter-sterilized and deionized water (Milli-Q), applied to a $Si_3N_4$ window with a micropipette, and air-dried. Additional standard spectra were recorded for pure yeast-derived fungal cell wall material and bacteria (*Escherichia coli*). Fungal cell wall material was prepared as described above and *E. coli* was grown on nutrient broth for 24 h. In preparation for STXM analysis, fungal and bacterial cell materials were washed twice with Milli-Q water and 2 μL of cell suspension was air-dried on $Si_3N_4$ windows. For each standard, three spectra were acquired from regions with optical densities <1.5 (to minimize saturation of the spectral features) and averaged.

Table 1
Quantification of relative proportions of organic functional groups in 1s C NEXAFS spectra by Gaussian peak deconvolution.

| | Aromatic C | Phenolic C | Aliphatic C | Carboxyl C/amide C | O-alkyl C | Carbonyl C | Aromaticity[b] | O-alkyl/ aromatic C[c] |
|---|---|---|---|---|---|---|---|---|
| Photon energy (eV) | 284–285.5 | 286.5–287 | 287.1–287.8 | 288.0–288.8 | 289–289.5 | 290–290.5 | | |
| *(a) Chemical changes in $^{15}$N-labeled materials (% abundance of functional groups[a])* | | | | | | | | |
| Original fungal cell wall material | 9(1) | 1(0) | 11(1) | 27(1) | 46(2) | 7(1) | 0.34 | 4.95 |
| Fe-associated OM ($^{15}$N-enriched) ($n = 3$) | 10(1) | 12(0) | 15(0) | 35(2) | 24(1) | 4(1) | 0.30 | 2.31 |
| *(b) Chemical changes in spectral types (% abundance of functional groups[a])* | | | | | | | | |
| Type 1 ($n = 3$) | 13(2) | 16(3) | 9(2) | 32(3) | 27(2) | 4(2) | 0.41 | 2.08 |
| Type 2 ($n = 6$) | 11(0) | 13(3) | 12(1) | 35(3) | 26(1) | 3(2) | 0.31 | 2.36 |
| Type 3 ($n = 7$) | 9(1) | 11(1) | 16(1) | 36(2) | 25(1) | 3(1) | 0.24 | 2.89 |
| Type 4 (mineral surfaces ($n = 5$) | 5(3) | 9(1) | 19(2) | 38(1) | 24(1) | 5(1) | 0.13 | 3.19 |

[a] Numbers are mean values reported with standard error in parentheses.

[b] Aromaticity index = (aromatic C)/(carboxyl and amide C).

[c] O-alkyl/aromatic C = ratio of% O-alkyl to aromatic C.

### *2.2.2. Data processing*

Stack images were aligned via a spatial cross-correlation analysis, clean areas of the $Si_3N_4$ membrane were used to normalize the transmission signal obtained from analyzed ROIs, and NEXAFS spectra were extracted from groups of pixels from ROIs using the aXis 2000 software package (Hitchcock, 2009).

Extracted C and N 1s NEXAFS spectra were normalized using the Athena software package for X-ray absorption spectroscopy (Ravel and Newville, 2005). Edge step normalization was performed using $E_0$ values of 290 eV and 408 eV for C and N NEXAFS, respectively. NEXAFS spectra were normalized across the full recorded range (278–330 for C 1s and 390–440 eV for N 1s). Peak assignments can be found in the figure captions.

A semi-quantitative analysis of C 1s NEXAFS spectra extracted from distinct features in the sample (such as fungal hyphae, bacteria, and mineral surfaces discussed as 'types' in the results section) was carried out by peak deconvolution using the software PeakFit (SeaSolve Software Inc., San Jose, CA, USA). Peak positions were assigned according to conventions reported by Schumacher et al. (2005) and Solomon et al. (2005). The deconvolution procedure was applied using Gaussian transitions with parameters as described in Kleber et al. (2011). No restrictions were placed on the Gaussian peaks and the final FWHM values and energy positions (Fig. A2, Appendix). Peak magnitude and energy for all Gaussian transitions were allowed to vary freely, allowing the peak positions to constrain themselves to the ranges given in Table 1.

## 2.3. High-resolution secondary ion mass spectrometry imaging

### *2.3.1. Imaging analysis*

Isotopic and chemical images were acquired on a NanoSIMS 50 (Cameca, Gennevilliers, France) at LLNL. This instrument allows the simultaneous imaging of five isotopes with high spatial resolution (up to 50 nm) and high mass resolution. For this study, electron multiplier (EM) detectors were positioned to collect $^{12}C^-$, $^{13}C^-$, $^{12}C^{14}N^-$, $^{12}C^{15}N^-$, and $^{56}Fe^{16}O^-$ ions. Due to the poor yield of $N^-$ under the $Cs^+$ primary beam, nitrogen was detected as the molecular ion $CN^-$, and iron was detected using its oxide ion ($^{56}Fe^{16}O^-$). The secondary mass spectrometer was tuned for >6800 mass resolving power (defined as the ratio $M/\Delta M$) in order to resolve isobaric interferences.

Ion images of the ROIs previously imaged by STXM were generated with a 1.5 pA $Cs^+$ primary beam, focused to a spot size of 120 nm, and stepped over the sample in a 256 × 256 pixel raster. Dwell time was 1 ms/pixel, and raster size was 10 × 10 μm. Secondary ions were detected in simultaneous collection mode by pulse counting to generate 60–180 serial quantitative secondary ion images (or 'layers'). No pre-analysis sputtering was done on these samples as we hypothesized that chemistry of interest might exist as thin layers on components of the sample (i.e., mineral particles). The electron flood gun was used for all analyses to avoid charging effects (Pett-Ridge and Weber, 2011).

A series of forty additional high-resolution NanoSIMS images (without corresponding STXM analysis) were collected to determine the isotopic enrichment of a larger number of soil particles, and to assess whether there was a spatial correlations between Fe-rich phases and $^{15}$N enrichment. Forty 10 × 10 μm (256 × 256 pixels) images were collected at random locations on the aforementioned specimens. Images were generated using the NanoSIMS settings described above.

### *2.3.2. Data processing*

NanoSIMS image data were processed as quantitative isotopic ratio images using the L'image software package developed by L. Nittler (Carnegie Institution of Washington), and were corrected for effects of quasi-simultaneous arrival (QSA), detector dead-time and image shift from layer to layer (due to drift in the location of the ion beam from frame to frame). Data planes collected before sputtering equilibrium was achieved (typically 5–10) were discarded. The isotopic composition ($\delta^{13}C$ and $\delta^{15}N$) of each ROI was calculated by averaging over all replicate layers where both C and N isotopes were at sputtering equilibrium. $\delta^{13}C$ and $\delta^{15}N$ were calculated as follows:

$$\delta^{a}X = \left(\frac{R_m}{R_{STD}} - 1\right) \times 1000\ [‰] \tag{1}$$

where $R_m$ is the isotopic ratio of the sample and $R_{STD}$ that of the reference standard. Repeated NanoSIMS analyses of a *Bacillus subtilis* spore preparation were used as a reference standard for the C and N isotopic measurements ($\delta^{13}C = -14.4‰$; $\delta^{15}N = 12.3‰$) (Kreuzer-Martin and Jarman, 2007). Isotopic enrichment of standards was independently determined at the University of Utah and used to normalize sample analysis as described previously by (Finzi-Hart et al., 2009). $^{56}Fe^{16}O^{-}/^{12}C^{-}$ ratios were used to localize Fe in the sample.

For those analysis locations analyzed by both SIMS and STXM imaging, ROIs for NanoSIMS data analysis were drawn based on the morphology of individual features using L'image. For the forty additional randomly-located NanoSIMS images, ROIs were drawn around discrete Fe-rich particles defined using two thresholds: Fe-rich particles with (i) average $^{56}Fe^{16}O^{-}/^{12}C^{-}$ ion ratios greater than 0.05 and (ii) pixel sizes between 200 and 5000 (i.e., total areas between 0.3 and 7.5 $\mu m^2$). These thresholds were based on the STXM characterization of three randomly located Fe (hydr)oxides in the sample, which all had $^{56}Fe^{16}O^{-}/^{12}C^{-}$ ratios $\geqslant 0.03$ and particles sizes ranging from ~1 to 2.5 $\mu m^2$. For comparison, ROIs of the remaining (mostly organic) soil particles were defined as those particles with $^{56}Fe^{16}O^{-}/^{12}C^{-}$ ratio values >0.001 and <0.03.

## 3. RESULTS

### 3.1. Selection of regions of interest (ROIs)

SEM mapping of the prepared samples indicated that 20–150 μm long hyphal structures associated with periodic clusters of minerals, organic matter and microbial residue were common features. The six hyphae-associated microstructures were analyzed for C, N and Fe speciation using STXM/NEXAFS and subsequently for $^{15}N$ and $^{13}C$ enrichment (to locate added isotopically enriched fungal cell wall material) using the more destructive NanoSIMS imaging technique. We did not observe any specific locations where $^{13}C$ was significantly enriched above natural abundance, but noticed slightly enriched $^{13}C$ values uniformly distributed across all analyzed areas (data not shown). However, three of the STXM/SIMS sample locations had areas with $^{15}N$ enrichment above background levels and are discussed further.

### 3.2. NanoSIMS imaging of the $\delta^{15}N$ and Fe distribution

NanoSIMS imaging was used to reveal general patterns in the distribution of $^{15}N$-enriched fungal cell wall material and potential transformation products within the sample collected after 3 weeks of incubation. General morphologies as well as the $^{15}N$ and Fe distribution within the three sample locations chosen for the combined imaging analysis are shown in Fig. 1. Transmission maps of the three locations show the same morphological patterns. In general, fungal hyphae are surrounded by soil particles (identified as mineral particles, amorphous organic matter, microbial residue in Section 3.3). Comparable morphological features were observed in preparations of samples collected after 1 and 2 weeks of incubation (see Fig. A1 in Appendix). Comparison of $\delta^{15}N$ and Fe distribution maps for the three locations shows that the spots with greatest enrichment of $^{15}N$ tend to coincide with Fe-rich particles.

### 3.3. STXM/NEXAFS characterization of $^{15}N$-enriched features on Fe-rich surfaces

STXM/NEXAFS spectromicroscopy was used to investigate the C and N chemistry of $^{15}N$-enriched OM associated with Fe-rich particles and the chemical form of Fe present. To this end, C, N and Fe NEXAFS spectra were extracted from $^{15}N$-enriched ROIs (white arrows in Fig. 1). Averaged NEXAFS spectra of $^{15}N$-enriched organic matter on Fe-rich particles (=Fe-associated OM) and additional reference materials are shown in Fig. 2 and are described below.

#### 3.3.1. C NEXAFS spectroscopy

The average C NEXAFS spectrum of the original fungal cell wall material consists of peaks representing signals of aromatic (a), aliphatic (c), carboxyl/amide (d) and O-alkyl (e) carbon (Fig. 3A). The predominance of the O-alkyl and carboxyl/amide C peak indicates the presence of β-1,3-glucan and NAG units in the cell wall, whereas aromatic C may originate from glycoproteins. Comparison of spectra extracted from the original fungal cell wall material to the $^{15}N$-enriched OM found on Fe-rich soil particles after 3 weeks of incubation reveals substantial changes (Fig. 2A). These changes could be due to a strong background of native organic materials coating the Fe-rich particle and/or substantial chemical transformations of the original material over the course of the incubation.

Spectral deconvolution of C NEXAFS spectra from the original and the $^{15}N$-labeled Fe-mineral associated OM shows the changes in functional group abundance that occurred over the course of the soil incubation (Table 1a). The most prominent change includes a strong decrease of O-alkyl C abundance associated with polysaccharides, such as β-1,3-glucan, with a simultaneous increase in carboxyl/amide C corresponding to proteinaceous materials. A change was also observed for aliphatic and phenolic C, which is notably more abundant on the Fe-rich particles. This might indicate a preferential association of lipid material with hydroxylated Fe oxide surfaces, or could have risen from the complexation of carboxylic groups with Fe or other metals on the surface (Plaschke et al., 2005; Armbruster et al., 2009). However, the increase in phenolic C also suggests that native organic matter derived from plants represents a substantial fraction of the organic coating found on these surfaces.

In order to gain insights into the molecular form of $^{15}N$-enriched compounds found on Fe-rich particles, we

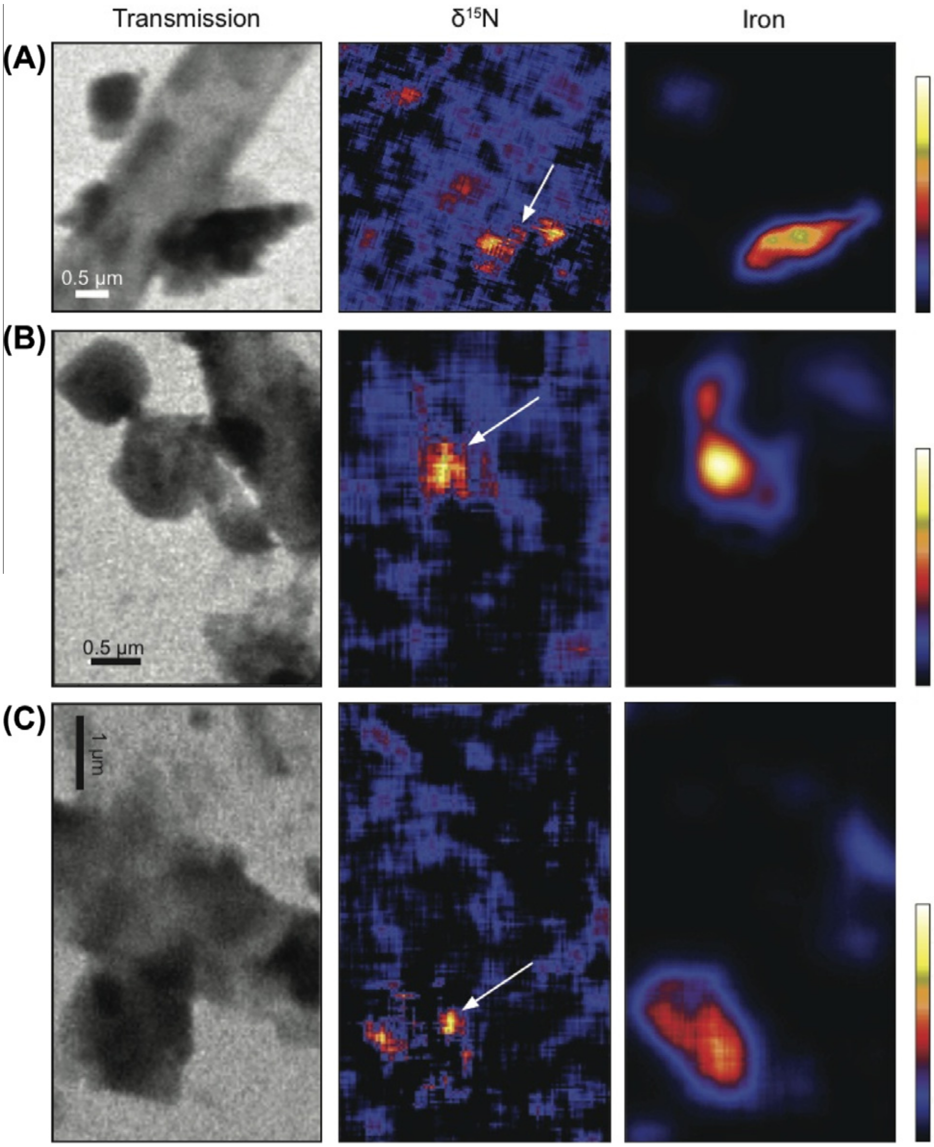

Fig. 1. Three hyphal-associated microstructures investigated by NanoSIMS imaging and STXM/NEXAFS spectromicroscopy: panels A, B and C show (i) STXM optical density maps of the three microstructures recorded at 300 eV and the corresponding heat maps for (ii) $\delta^{15}$N and (iii) Fe across the entire feature generated using $^{12}C^{15}N^-/^{13}C^{14}N^-$ and $^{56}Fe^{16}O^-/^{12}C^-$ secondary ion counts, respectively.

compared average spectrum of $^{15}$N-enriched Fe-associated OM to pure standards of individual fungal cell wall components (amino sugars, polysaccharides and protein). The spectra corresponding to Fe-associated OM show less intensity for peaks associated with polysaccharides (e) and greater intensity for peaks observed in proteinaceous materials (d) (Fig. 2A). Finally, there is a striking similarity between the reference spectra of purified bacterial cells and the spectra obtained from Fe-associated OM.

### 3.3.2. N NEXAFS spectroscopy

Comparing the N NEXAFS of fungal cell wall material to averaged spectra of the mineral-associated OM provides evidence for the chemical transformations of the starting material over the course of the incubation (Fig. 3B). The spectral peak at 401.7 eV (b) dominating spectra of fungal cell wall material is less pronounced and shifted to lower energies (401.5 eV) in spectra corresponding to mineral-associated N. This peak is commonly attributed to amide N (Mitra-Kirtley et al., 1993; Gillespie et al., 2009; Cody et al., 2011), but may contain contributions of pyrrolic and nitro N (Leinweber et al., 2007). The same peak also dominates the average N NEXAFS spectrum of the Fe-associated OM. Lower energy resonances (399–401 eV) were not interpreted due to the larger variability and potential artifacts related to damage induced by the X-ray beam (Leinweber et al., 2007).

The dominant resonance at 401.5 eV can be indicative of amide N from fungal amino sugars, peptides from microbial proteins (see references spectra in Fig. 2B), or nucleotides in DNA/RNA (reference spectra in Leinweber et al. (2007) and Mitra-Kirtley et al. (1993)). Due to these overlapping signals, our N NEXAFS spectra cannot conclusively determine whether the organic N in the Fe-associated OM is derived from amino sugars, protein and/or DNA/RNA. However, the N NEXAFS standard spectrum for bacterial cells shows very similar spectral patterns as those observed for Fe-associated OM. Since Fe-particle associated C appears to be of bacterial origin as suggested above, it is reasonable to assume that $^{15}$N-enriched spots of N on Fe particle surfaces are likely derived from a microbial source.

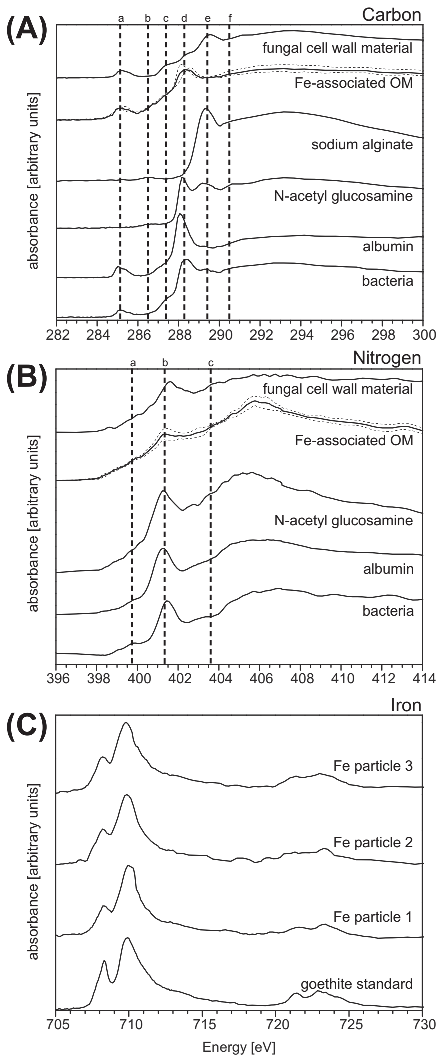

Fig. 2. Near edge X-ray absorption fine structure (NEXAFS) spectra extracted from the $^{15}$N-enriched regions on the Fe-rich particle surfaces. Averaged and normalized NEXAFS spectra of these locations collected at the C (A) and N (B) 1s absorption edge are compared to reference spectra of an amino sugar (N-acetyl-glucosamine, the monomer of fungal chitin), polysaccharide (alginate), protein (bovine serum albumin) and bacterial cells (*E. coli*). NEXAFS spectra collected at the Iron 2p absorption edge (C) are compared to reference spectra of goethite ($\alpha$-FeOOH). Average spectra are shown as mean ± standard deviation to this mean. Average spectra were obtained by calculating the mean at each energy value with $n$ = number of spectra. (A) Carbon 1s absorption edge peaks are identified as C = C 1s–$\pi^*$ transition of aromatic C at 285.1 eV (a), 1s–$\pi^*$ transition of C$\equiv$C in ene-ketone at 286.7 eV (b), 1s–3p/$\sigma^*$ transition of aliphatic C at 287.4 eV (c), 1s–$\pi^*$ transition of carboxylic and/or amide C at 288.3 eV (d), the 1s–3p/$\sigma^*$ transition of alcohol C–OH at 289.4 eV (e), and the 1s–$\pi^*$ transition of carbonyl C at 290.3 eV (f) (Cody et al., 1998; Schumacher et al., 2005; Solomon et al., 2005, 2009; Cody et al., 2011; Kleber et al., 2011). (B) Nitrogen 1s absorption edge peaks are identified as imine N 1s–p$^*$ transition at 399–400 eV (a), amide N 1s–3p/p$^*$ transition at 401.3 eV, and nitro N 1s–$\pi^*$ transition at 403.6 eV (c) (Cody et al., 2011). (C) Iron 2p absorption spectra consist of two main features associated with transitions from the 2p$_{3/2}$ (L3, ~710 eV) and 2p$_{1/2}$ (L2, ~721 eV) core levels. Absorbance was normalized at the location of the low-energy peak (709.8 eV).

### 3.3.3. Fe NEXAFS spectroscopy

Fe 2p NEXAFS spectra provide information on the oxidation state of Fe (van Aken and Liebscher, 2002). Fe 2p NEXAFS spectra acquired from $^{15}$N enriched mineral particles have spectral signatures that mirror that of a Fe (hydr)oxide standard (goethite) (Fig. 2C). As the observed intensity ratio between the higher energy (709.8 eV) and lower energy (708.0 eV) mimics that of the Fe(III) standard and there is no obvious absorbance in the expected Fe(II) energy range (707.5 eV), it appears that the mineralogy of this sample is dominated by Fe(III). Fe NEXAFS image scans of other mineral particles found within the three sample locations with noticeably less $^{15}$N enrichment showed little or no sign of Fe. However, difference maps across the Si and Al K-edges revealed greater concentrations of Si and Al in these particles (data not shown).

In summary, organic matter derived from $^{15}$N-labeled fungal cell wall materials appears to be preferentially associated with surfaces of Fe (hydr)oxide minerals in amide N form and has a C signature consistent with that of microbial residues.

## 3.4. STXM/NEXAFS characterization of spatial and chemical patterns in hyphae-associated microstructures

To test whether morphological and chemical patterns observed within the three soil microstructures provide additional insights into general transformation pathways of native hyphal material (and the amino sugars therein), general patterns in the micro-scale C and N dynamics were analyzed using the STXM/NEXAFS image data. A total of 21 C and N NEXAFS spectra were extracted for all structurally discernable features observed in the three imaged sample locations (see Fig. 3A for ROIs).

### 3.4.1. C NEXAFS spectroscopy

Close comparison of recurring patterns in the 21 C NEXAFS spectra extracted from all three sample locations showed that they could be grouped into four distinct spectral types (Fig. 4B). Morphological and chemical characteristics of each type are as follows:

(1) Type 1 spectra (grey) represent fungal hyphae and are dominated by peaks corresponding to aromatic C (a), phenolic C (b), carboxyl/amide C (d), and O-alkyl (e) (Fig. 3B). In the absence of other aromatic compounds, aromatic C is derived from proteina-

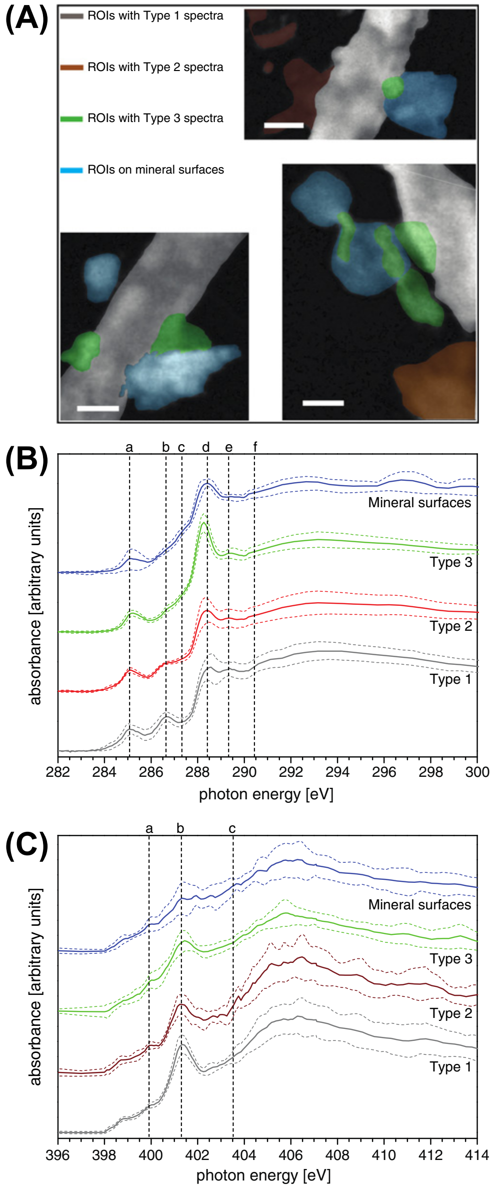

Fig. 3. Allocation of normalized C and N near edge X-ray absorption fine structure (NEXAFS) spectra to four typical signal patterns ("Types"). (A) Optical density map of hyphal-associated microstructures with colored regions of interest (ROIs) from which NEXAFS spectra at the C 1s absorption edge and the N 1s absorption edge were collected. ROIs are color-coded according to the spectral types extracted from them: Type 1 (grey), Type 2 (brown), Type 3 (green) and mineral surfaces (blue). Type 1 was designated as intact fungal hyphae, Type 2 as decomposing hyphal residue, Type 3 as microbial residue, and Type 4 as Fe-particle associated OM). Scale bar = 1 μm. For each of the four types of spectra identified we show the C 1s absorption edge spectra (B) and N 1s absorption edge spectra (C). C and N 1s absorption edge peaks are identified as described in the caption to Fig. 2. All plots show normalized and averaged spectra ± standard deviation. Average spectra were obtained by calculating the mean at each energy value with $n$ = number of spectra ($n_{\text{Type 1}} = 3$; $n_{\text{Type 2}} = 6$; $n_{\text{Type 3}} = 7$; $n_{\text{mineral surfaces}} = 5$). (For interpretation of the references to color in this figure legend, the reader is referred to the web version of this article.)

ceous cell wall components and/or melanin-like compounds, while amide C functionalities have their origin in chitin constituents of fungal cell walls. Phenolic peaks likely arise from fungal melanin and/or surface-associated phenols which tend to coat the fungal mycelium during the breakdown of lignin (Chua et al., 1983; Perez and Jeffries, 1992; Tian et al., 2003; Zhong et al., 2008).

(2) Type 2 spectra (brown) are associated with amorphous organic residues surrounding the fungal hyphae and mineral particles. These spectra show strong similarity to those identified as Type 1, but originate from objects that lack the straightforward morphology of fungal hyphae.

(3) Type 3 spectra (green) were extracted from small ROIs in the immediate vicinity of hyphal structure and mineral particles. These spectra show dominant resonances in the aromatic C region (a), followed by a steep rise in the carboxyl/amide C region (d). The overall spectral signature is that of microbial tissues and proteins (see Fig. 3A, also: Toner et al. (2009)), implying that this spectral type represents OM composed of microbial biomass or material that has been processed by a microbial metabolism.

(4) The fourth spectral type (blue) was derived from OM bound to mineral surfaces (=mineral-associated OM). Comparing Type 4 to Types 1–3 is of interest because the latter represent potential sources for the surface-associated OM. Type 4 spectra differ substantially from Type 1 and 2 spectra, and exhibit the same microbial signature as Type 3 with the exception of two subtle differences. These are a slightly lower aromatic C signal (letter "a" in Fig. 4B) and a slightly stronger O-alkyl C signal (e) relative to that of carboxylic C/amide N (d). These differences suggest that this mineral-associated OM is derived from microbial materials or residues (similar to Type 3), and that the contributions from Types 1 and 2 (hyphae dominated) are minor.

Deconvolution of the C NEXAFS spectra showed significant chemical changes across the four distinct features (or 'Types') of the sample (Table 1b). First, the relative proportion of carbonyl C remains relatively constant going from Type 1 to Type 4 spectra, with a concomitant decrease in O-alkyl C. Second, the relative amounts of carboxyl C/amide C and aliphatic C increase from Type 1 though 4, with surface-bound OM having the highest contribution. Finally, the relative proportions of aromatic and phenolic C declined from Type 1 to 3, and are lowest in those organic materials that are attached to mineral surfaces (Table 1).

Along the sequence from Type 1 to mineral-associated Type 4 materials, there is a consistent evolution of the functional group composition (Fig. 4A). The abundance of aliphatic C progressively increases until it peaks on mineral surfaces where it is more than double relative to Type 1 materials. In contrast, aromatic and phenolic C abundances gradually decline to less than half of the Type 1 value (−68% and −47%, respectively).

### *3.4.2. N NEXAFS spectroscopy*

In the corresponding N NEXAFS spectra of the four spectral types described above (Fig. 4C), a broad absorption band at 401–402 eV, originating from amide N, dominates all four types. This amine N peak is more pronounced in Types 1 and 2 than in Type 3, suggesting some depletion of amide N may have occurred during the progression from Type 1 to Type 3 materials. The average N NEXAFS spectrum of mineral-associated OM shows a less pronounced amide N peak. Lines indicating the standard deviation suggest a substantial variation in abundance and form of N on these surfaces (Fig. 4C). In contrast to the average spectrum of Fe-associated OM (Fig. 2; extracted from small $^{15}$N-enriched patches in Fe hydroxide surfaces), this spectrum was averaged across five minerals. It is possible to assume that some of the variability in the results is related to differences in mineral surface chemistry.

## 3.5. Characterization of the $\delta^{15}$N and Fe distribution of distinct morphological and chemical features

NanoSIMS imaging of the STXM locations described above was used to measure $^{15}$N enrichment as a function of Fe abundance across the four distinct morphological and chemical features (or 'Types') (Fig. 5A). All four types were enriched in $^{15}$N relative to unlabeled bulk soil and the extracted microbial biomass (Fig. 5A, solid lines). Among the four particle types, Fe abundance increased, with Type 1 < Type 2 < Type 3 < Type 4. Along the same trajectory average $\delta^{15}$N values showed a steep increase from Type 1 (intact hyphae) and Type 2 (decomposing hyphae) to Type 3 (microbial residue), before increasing more moderately to Type 4 (mineral-associated OM) following a log relationship ($R^2 = 0.81$, $p < 0.05$) (Fig. 5). The elevated enrichment for Type 3 (microbial residue) were in agreement with our isotopic data for enriched bulk soil showing $^{15}$N enrichment of the microbial biomass relative to the whole soil (Fig. 5, dashed lines).

In addition, $\delta^{15}$N values were extracted from local $^{15}$N-hotspots on Fe-rich particles previously analyzed by STXM and NanoSIMS (Fig. 1, white arrows). These values tended to be larger than those of Type 3 (microbial residue) and Type 4 (mineral-associated OM), and are correlated with Fe abundance ($R^2 = 0.98$, $p < 0.05$) (Fig. 5B).

In order to substantiate the relationship between $^{15}$N enrichment and Fe abundance, 30 additional Fe-rich particles in 40 randomly selected 10 × 10 μm images were analyzed by NanoSIMS. In this larger dataset, Fe-rich particles were significantly enriched in $^{15}$N compared to the remaining soil particles ($p < 0.05$, two-tailed $t$-test) (Fig. 5C).

## 4. DISCUSSION

Our combined imaging mass spectrometry and STXM/NEXAFS results suggest that in the vicinity of fungal hyphae and associated soil microstructures, $^{15}$N-labeled amide N, derived from fungal cell wall material, preferentially associates with Fe (hydr)oxide surfaces or Fe-OM co-precipitates on the surface of other minerals. After 3 weeks of incubation we found no significant $^{13}$C-enrichment suggesting that much of the C in the initial substrate may have become mineralized. The chemistry of $^{15}$N-enriched Fe-associated spots, however, was dramatically altered compared to the initial substrate and took on a spectral signature that is consistent with bacterial cells. The combination of C and N NEXAFS data further indicate that amide N found on mineral surfaces stems from bacterial protein rather than amino sugars or nucleotides. This suggests that the fungal cell wall material may have been rapidly metabolized prior to partitioning onto the mineral surfaces.

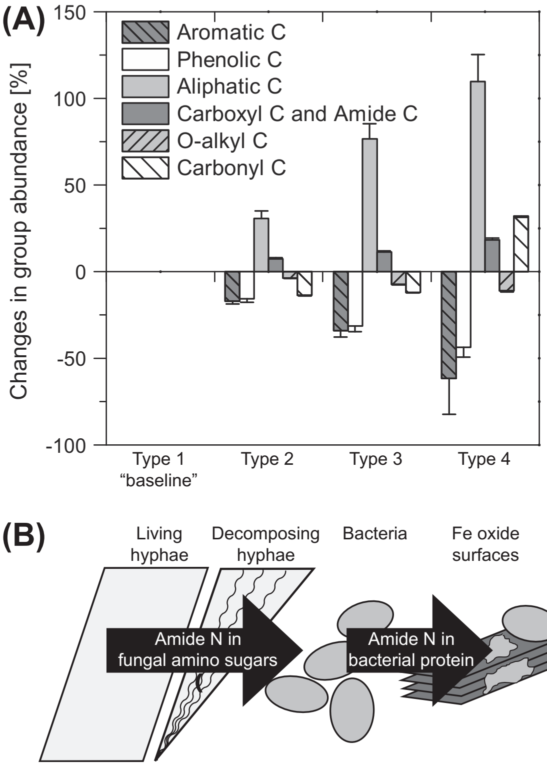

Fig. 4. (A) Percent changes in the relative abundance of functional groups across the four spectral 'Types' as defined in Fig. 2A. Calculations were based on a proposed model that assumes that Type 1 material becomes transformed into Types 2, 3, and 4 materials during sequential microbial processing. Hence, percent changes in functional group abundance are expressed relative to Type 1 material ('baseline'). Mean values ± SE are reported. (B) Proposed model for microbial amide N cycling in the soil matrix adjacent to fungal hyphae. The chemical composition of organic C at each processing step corresponds to that depicted in (A).

## 4.1. Microbial C cycling in hyphal-dominated microenvironments

General patterns of C and N dynamics within the three sample locations were resolved by categorizing similar chemical and morphological features into four distinct types. The chemical trends observed in the four spectral types can be rationalized by assuming that (i) Type 1 spectra represent fungal hyphae surrounded by dead hyphal residues (Type 2) that lost their morphological structure due to initial decomposition processes, but still consist of the same chemical components, (ii) Type 3 spectra reflect microorganisms or microbial residue associating with the hyphae, and (iii) OM associated with minerals represent an endpoint (Type 4) where selected microbial components derived from Type 3 accumulate (Fig. 4B).

The model we propose for chemical transformations of the added cell wall biomass is supported by the strongly microbial C chemistry in Type 3 and 4 features, which are dominated by the aliphatic C of cell membrane phospholipids and carboxyl/amide C of proteins in bacterial cells (Lengeler et al., 1999). The chemical trends not only indicate that mineral-associated OM is mostly of bacterial origin (Type 3), but also that certain chemical components (aliphatic C) become selectively enriched on mineral surfaces relative to their origin, while others (aromatic and phenolic C) are depleted. Spectra of this kind have been reported for organic materials rich in proteins and aliphatics on marine particles (Brandes et al., 2004) and in soil microaggregates (Lehmann et al., 2006; Kleber et al., 2011).

### 4.2. Microbial amide N cycling in hyphal-dominated microenvironments

In hyphal dominated soil environments, transformation pathways of amino sugar N appear to be directly linked to the C dynamics that we discuss above. Assuming that mineral surface-associated C is of bacterial origin, we can reasonably assign the $^{15}$N-enriched spots of amide N on the mineral surface to microbial residues as well. This suggests that amide N from amino sugars is initially assimilated by hyphal-associated bacteria, and subsequently re-synthesized into bacterial proteins before adsorbing to Fe (hydr)oxide surfaces of co-precipitation with Fe (hydr)oxide. That amide N from microbial proteins becomes concentrated by Fe (hydr)oxides may also be a result of associations that occur after cell lysis, through trapping of extracellular enzymes, or adhesive interactions of cell wall proteins during bacterial colonization (Rillig et al., 2007) (Fig. 4B). In our incubation, amide N may have become concentrated (relative to C) due to microbial assimilation of the added fungal cell wall N. This conclusion is supported by the fact that low levels of $^{13}$C appeared to be dispersed uniformly through the sample, whereas $^{15}$N was found in concentrated patches.

Our micro-scale observations of microbial assimilation of amide N in fungal cell wall material within a relatively short incubation period of 3 weeks concurs with previous reports suggesting fungal amino sugars act as an N source for microbiota in N-deficient forest soil ecosystems (Olander and Vitousek, 2000; Zeglin et al., 2012). Standard bulk analyses can only account for the fraction of the added N that becomes assimilated (biomass N pool) or mineralized (inorganic N pool). What is not accounted for by these methods is generally assumed to be either (i) N that was never modified by microbial activity or (ii) N from the cell wall material that was so fully transformed that it could not be detected in mineralized or assimilated pools. Our results suggest that some of this remaining amide N has undergone significant microbial transformations, and that the association of this residual amide N with Fe-minerals may often escape detection by bulk analyses. The fact that this unaccounted microbial amide N is preserved on Fe-rich mineral surfaces also suggests that N cycling in N-limited systems may be controlled in part by the presence of Fe (hydr)oxides or other mineral adsorbents with similar surface properties.

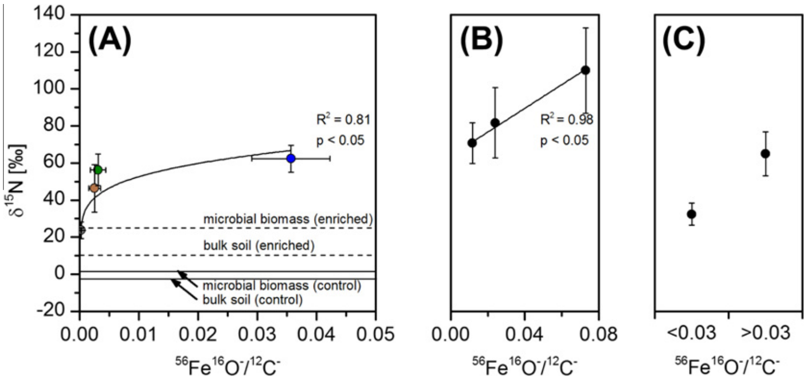

Fig. 5. (A) Average $^{15}$N enrichment as a function of Fe abundance for defined 'Types' of structures within the three heterogeneous soil microstructures analyzed by NanoSIMS imaging. Data points are color-coded according to the spectral types extracted from them: Type 1 (grey), Type 2 (brown), Type 3 (green) and Type 4 (blue). The reader is referred to Section 3.3 for additional discussion of these types. Given values for $\delta^{15}$N and Fe represent averaged $^{12}$C$^{15}$N$^-$/$^{13}$C$^{14}$N$^-$ and $^{56}$Fe$^{16}$O$^-$/$^{12}$C$^-$ ion ratios, respectively, of entire ROIs and do not account for the within-feature variability (e.g., as is evident on the surface of the large mineral particles in Fig. 1). Mean values ± SE are given for each Type ($n_{\text{Type 1}} = 3$; $n_{\text{Type 2}} = 3$; $n_{\text{Type 3}} = 4$; $n_{\text{mineral surfaces}} = 3$). Average $\delta^{15}$N values of whole soil and chloroform-extracted microbial biomass of soil incubated over the 3-week time period are drawn as horizontal lines. For comparison, values for soils amended with $^{15}$N-labeled cell wall material (enriched) and unlabeled cell wall materials (control) are provided. (B) Average $^{15}$N enrichment as a function of Fe abundance for 'hotspots' located on the three Fe-rich particles shown in Fig. 1 (white arrows). Mean values ± SE are reported for each ROI ($n = 20$). (C) $^{15}$N enrichment of soil particles detected in 40 randomly selected 10 × 10 μm images analyzed by NanoSIMS. Fe-rich particles ($n = 30$) are defined as features with $^{56}$Fe$^{16}$O$^-$/$^{12}$C$^-$ ratios ⩾0.03 and particle sizes >0.3 μm², while all remaining, mostly organic soil particles ($n = 180$) are defined by $^{56}$Fe$^{16}$O$^-$/$^{12}$C$^-$ ratios between 0.001 and 0.03. Mean values ± SE are reported.

### 4.3. High affinity of Fe (hydr)oxides for microbial C and N

Our imaging investigation demonstrated that Fe (hydr)oxide surfaces or co-precipitates act to concentrate aliphatic C derived from microbial lipids as well as amide C and N from bacterial protein, and suggests that such associations can form on a very short time scale. Both lipids and proteins are major components of bacterial extracellular polymeric substances (EPS) which both gram-positive and -negative bacteria exude EPS into the surrounding soil microenvironment (Davies, 1999), thereby coating exposed mineral surfaces. The formation of these 'conditioning films' is generally regarded as an adaptive strategy to colonize mineral surfaces (Roberson and Firestone, 1992; Davies, 1999). Various studies show that microbial lipids tend to be enriched in clay-sized soil mineral fractions (Baldock et al., 1992; Guggenberger et al., 1995; Clemente et al., 2011). One possible explanation is the large sorptive affinity of phospholipids to the surfaces of clay-sized Fe (hydr)oxide minerals (Omoike et al., 2004; Parikh and Chorover, 2008; Cagnasso et al., 2010). For instance, Cagnasso et al. (2010) demonstrated the rapid formation of inner-sphere complexes between phosphate groups of bacterial cell membrane phospholipids and hydroxylated Fe oxide surfaces. Interactions of proteins with mineral surfaces are a long established phenomenon (Theng, 1979; Chevallier et al., 2003; Wershaw, 2004) and their roles in soil N cycling are discussed by Kleber et al. (2007) and Rillig et al. (2007). Omoike and Chorover (2006) showed that phosphorylated proteins in a mixture of extracellular polymeric substances preferentially adsorb to hydroxylated goethite surfaces via both inner-sphere and electrostatic interactions involving phosphate groups. The association of EPS with mineral surfaces via such sorptive interactions has been suggested to be the initial step in the formation of organo-mineral assemblages in soils (Chenu and Stotzky, 2002), which are widely seen as essential to soil C and N stability (Lehmann et al., 2006; Kögel-Knabner et al., 2008; Miltner et al., 2011).

## 5. CONCLUSIONS

Our high-resolution imaging investigation was focused on the microbial processing of biomaterials and the partitioning of newly synthesized microbial products onto hydroxylated surfaces in a real soil microenvironment, and suggests that associations of Fe (hydr)oxides with microbial residue can establish within very short time scales (3 weeks). In our experiment, a substantial fraction of the $^{15}$N-labeled amide N from chitinous fungal cell wall material entering this particular microenvironment – dominated by closely associated fungal hyphae, bacteria and minerals – became preferentially associated with Fe (hydr)oxide minerals. The spectral signatures of these OM-Fe associations match those of microbial biopolymers, particularly proteins and lipids. This implies that intensive microbial processing of the amino sugars occurred prior to association with the mineral surfaces. We hypothesize that this is because N from fungal amino sugars was assimilated and processed by hyphal-associated bacteria. It is possible that some of this amide N may not be continually recycled within the biomass pool, but instead may become concentrated and/or immobilized on Fe (hydr)oxides as microbial protein. Our results raise important questions regarding how associations of microbial N with Fe (hydr)oxide surfaces influences N cycling, specifically whether Fe surface immobilization of N affects its availability to microorganisms in these microenvironments: Is amide N bound irreversibly to these surfaces and rendered unavailable for microorganisms or is this surface-associated N part of a bioavailable 'conditioning film' that is actively promoted by microorganisms to serve a specific physiological pur-

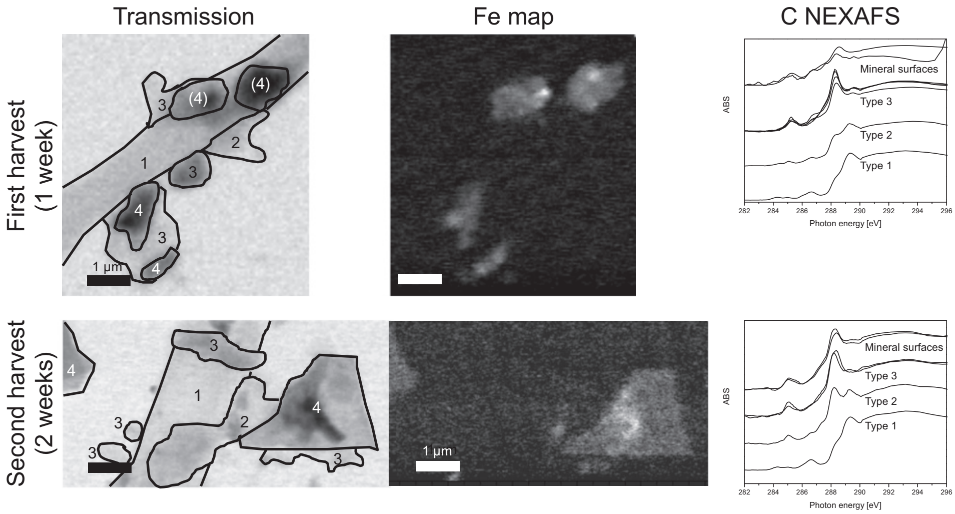

Fig. A1. Corresponding STXM transmission maps, Fe distribution map, and C NEXAFS spectra of hyphal-associated microstructures harvested after 1 and 2 weeks of incubation. Transmission was measured at 290 eV, Fe maps are based on difference maps of images taken above and below the edge (700 and 709 eV), and C NEXAFS are grouped into the four distinct 'Types' discussed in the main text. ROIs drawn in the transmission map indicate the origin of the spectra.

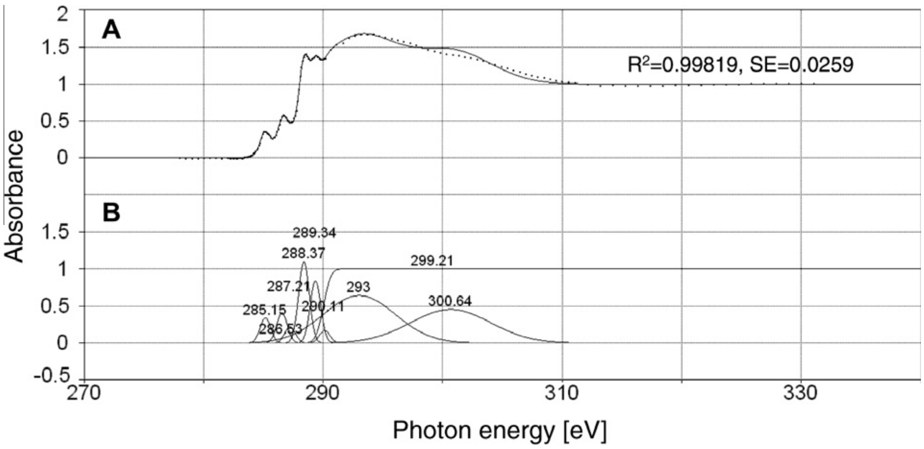

Fig. A2. Illustration of the Gaussian and arctangent functions used for the spectral deconvolution of C NEXAFS. (A) Sample spectrum taken from Type 1 (solid line) and the best fit (dashed line). (B) Positions of Gaussian and arctangent function producing the best fit in this example.

pose? Although the scope of this study is limited to organic layer horizons of a specific soil ecosystem, these issues are at the core of how we comprehend biotic and abiotic interactions that shape initial decomposition processes in soil and their implications for ecosystem functioning.

## ACKNOWLEDGMENTS

The authors thank A.L.D. Kilcoyne and T. Tyliszczak for their help and support at ALS beamlines 5.3.2.2 and 11.0.2, and K. Carpenter for assistance with SEM imaging at LLNL. M. Keiluweit acknowledges a Lawrence Scholar Fellowship awarded by LLNL. This work was performed under the auspices of the U.S. Department of Energy by Lawrence Livermore National Laboratory under Contract DE-AC52-07NA27344. Funding was provided by an LDRD "Microbes and Minerals: Imaging C Stabilization" at LLNL to J.P.R., and the work of P.S.N. is supported by LBNL award No. IC006762 as sub-award from LLNL and DOE-BER Sustainable Systems SFA. Funding for D.D.M. and L.H.Z. was provided by the National Science Foundation under Grant No. 0348689. The Advanced Light Source is supported by the Director, Office of Science, Office of Basic Energy Sciences, of the U.S. DOE under Contract No. DE-AC02-05CH11231.

## APPENDIX A

See Figs. A1 and A2.

## REFERENCES

Amelung W. (2003) Nitrogen biomarkers and their fate in soil. *J. Plant Nutr. Soil Sci.* **166**, 677–686.

Amelung W., Kimble J. M., Samson-Liebig S. and Follett R. F. (2001a) Restoration of microbial residues in soils of the Conservation Reserve Program. *Soil Sci. Soc. Am. J.* **65**, 1704–1709.

Amelung W., Miltner A., Zhang X. and Zech W. (2001b) Fate of microbial residues during litter decomposition as affected by minerals. *Soil Sci.* **166**, 598–606.

Armbruster M. K., Schimmelpfennig B., Plaschke M., Rothe J., Denecke M. A. and Klenze R. (2009) Metal-ion complexation effects in C 1s-NEXAFS spectra of carboxylic acids—evidence by quantum chemical calculations. *J. Electron Spectrosc.* **169**, 51–56.

Baldock J. A., Oades J. M., Waters A. G., Peng X., Vassallo A. M. and Wilson M. A. (1992) Aspects of the chemical structure of soil organic materials as revealed by solid-state $^{13}$C NMR spectroscopy. *Biogeochemistry* **16**, 1–42.

Brandes J. A., Lee C., Wakeham S., Peterson M., Jacobson C., Wirick S. and Cody G. (2004) Examining marine particulate organic matter at sub-micron scales using scanning transmission X-ray microscopy and carbon X-ray absorption near edge structure spectroscopy. *Mar. Chem.* **92**, 107–121.

Cabib E. and Bowers B. (1971) Chitin and yeast budding – localization of chitin in yeast bud scars. *J. Biol. Chem.* **246**.

Cagnasso M., Boero W., Franchini M. and Chorover J. (2010) ATR-FTIR studies of phospholipid vesicle interactions with alpha-FeOOH and alpha-$Fe_2O_3$ surfaces. *Colloids Surf. B: Biointerfaces* **76**, 456–467.

Chenu C. and Stotzky G. (2002) Interactions between microorganisms and soil particles: an overview. In *Interactions between Soil Particles and Microorganisms* (eds. P. M. Huang, J. M. Bollag and N. Senesi). Wiley, New York, pp. 3–40.

Chevallier T., Muchaonyerwa P. and Chenu C. (2003) Microbial utilisation of two proteins adsorbed to a vertisol clay fraction: toxin from *Bacillus thuringiensis* subsp. *tenebrionis* and bovine serum albumin. *Soil Biol. Biochem.* **35**, 1211–1218.

Chua M. G. S., Choi S. and Kirk T. K. (1983) Mycelium binding and depolymerization of synthetic $^{14}$C-labeled lignin during decomposition by *Phanerochaete chrysosporium*. *Holzforschung* **37**, 55–61.

Clemente J. S., Simpson A. J. and Simpson M. J. (2011) Association of specific organic matter compounds in size fractions of soils under different environmental controls. *Org. Geochem.* **42**, 1169–1180.

Cody G. D., Ade H., Wirick S., Mitchell G. D. and Davis A. (1998) Determination of chemical–structural changes in vitrinite accompanying luminescence alteration using C-NEXAFS analysis. *Org. Geochem.* **28**, 441–455.

Cody G. D., Gupta N. S., Briggs D. E. G., Kilcoyne A. L. D., Summons R. E., Kenig F., Plotnick R. E. and Scott A. C. (2011) Molecular signature of chitin-protein complex in Paleozoic arthropods. *Geology* **39**, 255–258.

Davies D. G. (1999) Regulation of matrix polymer in bio film formation and dispersion. In *Microbial Extracellular Polymeric*

*Substances* (eds. J. Wingender, T. R. Neu and H. C. Flemming). Springer, Berlin.

Eusterhues K., Rennert T., Knicker H., Kogel-Knabner I., Totsche K. U. and Schwertmann U. (2011) Fractionation of organic matter due to reaction with ferrihydrite: coprecipitation versus adsorption. *Environ. Sci. Technol.* **45**, 527–533.

Finzi-Hart J. A., Pett-Ridge J., Weber P. K., Popa R., Fallon S. J., Gunderson T., Hutcheon I. D., Nealson K. H. and Capone D. G. (2009) Fixation and fate of C and N in the cyanobacterium *Trichodesmium* using nanometer-scale secondary ion mass spectrometry. *Proc. Natl. Acad. Sci. USA* **106**, 6345–6350.

Gillespie A. W., Walley F. L., Farrell R. E., Leinweber P., Schlichting A., Eckhardt K. U., Regier T. Z. and Blyth R. I. R. (2009) Profiling rhizosphere chemistry: evidence from carbon and nitrogen K-edge XANES and pyrolysis-FIMS. *Soil Sci. Soc. Am. J.* **73**, 2002–2012.

Griffiths R. P., Caldwell B. A., Cromack K. and Morita R. Y. (1990) Douglas-fir forest soils colonized by ectomycorrhizal mats. *Can. J. For. Res./Rev. Can. Rech. For.* **20**, 211–218.

Guggenberger G., Frey S. D., Six J., Paustian K. and Elliott E. T. (1999) Bacterial and fungal cell-wall residues in conventional and no-tillage agroecosystems. *Soil Sci. Soc. Am. J.* **63**, 1188–1198.

Guggenberger G., Zech W., Haumaier L. and Christensen B. T. (1995) Land-use effects on the composition of organic-matter in particle-size separates of soil: 2. CPMAS and solution $^{13}$C NMR analysis. *Eur. J. Soil Sci.* **46**, 147–158.

Herrmann A. M., Clode P. L., Fletcher I. R., Nunan N., Stockdale E. A., O'Donnel A. G. and Murphy D. V. (2007) A novel method for the study of the biophysical interface in soils using nano-scale secondary ion mass spectrometry. *Rapid Comm. in Mass Spectro.* **21**, 29–34.

Hitchcock A. P. (2009) aXis200 Available from: <http://unicorn.mcmaster.ca/aXis2000.html/>.

Ingham E. R., Griffiths R. P., Cromack K. and Entry J. A. (1991) Comparison of direct vs fumigation incubation microbial biomass estimates from ectomycorrhizal mat and non-mat soils. *Soil Biol. Biochem.* **23**, 465–471.

Kaiser K. and Zech W. (2000) Sorption of dissolved organic nitrogen by acid subsoil horizons and individual mineral phases. *Eur. J. Soil Sci.* **51**, 403–411.

Kiem R. and Koegel-Knabner I. (2002) Refractory organic carbon in particle size fractions of arable soils: II. Organic carbon in relation to mineral surface area and iron oxides in fractions <6 μm. *Org. Geochem.* **33**, 1699–1713.

Kiem R. and Koegel-Knabner I. (2003) Contribution of lignin and polysaccharides to the refractory carbon pool in C-depleted arable soils. *Soil Biol. Biochem.* **35**, 101–118.

Kilcoyne A. L. D., Tyliszczak T., Steele W. F., Fakra S., Hitchcock P., Franck K., Anderson E., Harteneck B., Rightor E. G., Mitchell G. E., Hitchcock A. P., Yang L., Warwick T. and Ade H. (2003) Interferometer controlled scanning transmission X-ray microscopes at the Advanced Light Source. *J. Synchrotron Radiat.* **10**, LBNL-53202.

Kinyangi J., Solomon D., Liang B. I., Lerotic M., Wirick S. and Lehmann J. (2006) Nanoscale biogeocomplexity of the organo-mineral assemblage in soil: application of STXM microscopy and C 1s-NEXAFS spectroscopy. *Soil Sci. Soc. Am. J.* **70**, 1708–1718.

Kirchman D. and Clarke A. (1999) Hydrolysis and mineralization of chitin in the Delaware Estuary. *Aquat. Microb. Ecol.* **18**, 187–196.

Kirz J., Jacobsen C. and Howells M. (1995) Soft X-ray microscopes and their biological applications. *Q. Rev. Biophys.* **28**, 33–130.

Kleber M., Nico P. S., Plante A., Filley T., Kramer M., Swanston C. and Sollins P. (2011) Old and stable soil organic matter is not necessarily chemically recalcitrant: implications for modeling concepts and temperature. *Global Change Biol.* **17**, 1097–1107.

Kleber M., Sollins P. and Sutton R. (2007) A conceptual model of organo-mineral interactions in soils: self-assembly of organic molecular fragments into zonal structures on mineral surfaces. *Biogeochemistry* **85**, 9–24.

Kluber L. A., Tinnesand K. M., Caldwell B. A., Dunham S. M., Yarwood R. R. and Myrold D. D. (2010) Ectomycorrhizal mats alter forest soil biogeochemistry. *Soil Biol. Biochem.* **42**, 1607–1613.

Kögel-Knabner I., Guggenberger G., Kleber M., Kandeler E., Kalbitz K., Scheu S., Eusterhues K. and Leinweber P. (2008) Organo-mineral associations in temperate soils: integrating biology, mineralogy, and organic matter chemistry. *J. Plant Nutr. Soil Sci.* **171**, 61–82.

Kreuzer-Martin H. W. and Jarman K. H. (2007) Stable isotope ratios and forensic analysis of microorganisms. *Appl. Environ. Microbiol.* **73**, 3896–3908.

Lehmann J., Kinyangi J. and Solomon D. (2006) Organic matter stabilization in soil micro-aggregates: implications from spatial heterogeneity of organic carbon contents and carbon forms. *Biogeochemistry* **85**, 45–57.

Lehmann J., Liang B., Solomon D., Lerotic M., Luizaõ F., Kinyangi J., Schäfer T., Wirick S. and Jacobsen C. (2005) Near-edge X-ray absorption fine structure (NEXAFS) spectroscopy for mapping nano-scale distribution of organic carbon forms in soils: application to black carbon particles. *Global Biogeo. Cycle* 19, GB1013. http://dx.doi.org/10.1029/2004GB002435.

Leinweber P., Kruse J., Walley F. L., Gillespie A., Eckhardt K.-U., Blyth R. I. R. and Regier T. (2007) Nitrogen K-edge XANES – an overview of reference compounds used to identify 'unknown' organic nitrogen in environmental samples. *J. Synchrotron Radiat.* **14**, 500–511.

Lengeler J., Drews G. and Schlegel H. (1999) *Biology of the Prokaryotes*. Wiley-Blackwell.

Ma Y., Chen C. T., Meigs G., Randall K. and Sette F. (1991) High-resolution K-shell photoabsorption measurements of simple molecules. *Phys. Rev. A* **44**, 1848–1858.

Mikutta R., Kaiser K., Dörr N., Vollmer A., Chadwick O. A., Chorover J., Kramer M. G. and Guggenberger G. (2010) Mineral impact on organic nitrogen across a long-term soil chronosequence (0.3–4100 kyr). *Geochim. Cosmochim. Acta* **74**, 2142–2164.

Miltner A., Bombach P., Schmidt-Brücken B. and Kästner M. (2011) SOM genesis: microbial biomass as a significant source. *Biogeochemistry* **22**, 139–143.

Mitra-Kirtley S., Mullins O. C., Vanelp J., George S. J., Chen J. and Cramer S. P. (1993) Determination of the nitrogen chemical structures in petroleum asphaltenes using XANES spectroscopy. *J. Am. Chem. Soc.* **115**, 252–258.

Müller C. W., Kölbl A., Hoeschen C., Hillion F., Heister K., Herrmann A. M. and Kögel-Knabner I. (2012) Submicron scale imaging of soil organic matter dynamics using NanoSIMS—from single particles to intact aggregates. *Org. Geochem.* http://dx.doi.org/10.1016/j.orggeochem.2011.06.003.

Nelson D. W. and Sommers L. E. (1996) Total carbon, organic carbon, and organic matter. In *Methods of Soil Analysis: Part 3. Chemical Methods* (ed. D. L. Sparks). Soil Science Society of America Book Series, No. 5.

Olander L. P. and Vitousek P. M. (2000) Regulation of soil phosphatase and chitinase activity by N and P availability. *Biogeochemistry* **49**, 175–190.

Omoike A. and Chorover J. (2006) Adsorption to goethite of extracellular polymeric substances from *Bacillus subtilis*. *Geochim. Cosmochim. Acta* **70**, 827–838.

Omoike A., Chorover J., Kwon K. and Kubicki J. (2004) Adhesion of bacterial exopolymers to alpha-FeOOH: inner-sphere complexation of phosphodiester groups. *Langmuir* **20**, 11108–11114.

Parikh S. and Chorover J. (2008) ATR-FTIR study of lipopolysaccharides at mineral surfaces. *Colloids Surf. B: Biointerfaces* **62**, 188–198.

Perez J. and Jeffries T. W. (1992) Roles of manganese and organic-acid chelators in regulating ligin degradation and biosynthesis of peroxidases by *Phanerochaete chrysosporium*. *Appl. Environ. Microbiol.* **58**, 2402–2409.

Pett-Ridge J. and Weber P. K. (2011) NanoSIP: NanoSIMS applications for microbial biology. In *Microbial Systems Biology: Methods and Protocols* (ed. A. Navid). Humana Press.

Plaschke M., Rothe J., Altmaier M., Denecke M. A. and Fanghänel T. (2005) Near edge X-ray absorption fine structure (NEXAFS) of model compounds for the humic acid/actinide ion interaction. *J. Electron Spectrosc.* **148**, 151–157.

Ravel B. and Newville M. (2005) ATHENA, ARTEMIS, HEPHAESTUS: data analysis for X-ray absorption spectroscopy using IFEFFIT. *J. Synchrotron Radiat.* **12**, 537–541.

Rillig M. C., Caldwell B. A., Woesten H. A. B. and Sollins P. (2007) Role of proteins in soil carbon and nitrogen storage: controls on persistence. *Biogeochemistry* **85**, 25–44.

Roberson E. and Firestone M. (1992) Relationship between desiccation and exopolysaccharide production in a soil *Pseudomonas* sp.. *Appl. Environ. Microbiol.* **58**, 1284–1291.

Roff J., Kroetsch J. and Clarke A. (1994) A radiochemical method for secondary production in planktonic custacea based on rate of chitin synthesis. *J. Plankton Res.* **16**, 961–976.

Schumacher M., Christl I., Vogt R. D., Barmettler K., Jacobsen C. and Kretzschmar R. (2005) Chemical composition of aquatic dissolved organic matter in five boreal forest catchments sampled in spring and fall seasons. *Biogeochemistry* **80**, 263–275.

Sinsabaugh R. L., Antibus R. K., Linkins A. E., McClaugherty C. A., Rayburn L., Repert D. and Weiland T. (1993) Wood decomposition: nitrogen and phosphorus dynamics in relation to extracellular enzyme activity. *Ecology* **74**, 1586–1593.

Sodhi R. N. S. and Brion C. E. (1984) Reference energies for inner shell electron energy-loss spectroscopy. *J. Electron Spectrosc.* **34**, 363–372.

Soil Survey Staff, 2010. Keys to Soil Taxonomy. Natural Resource Conservation Service, USDA. Available from: <http://soils.usda.gov/technical/classification/tax_keys/>.

Solomon D., Lehmann J., Kinyangi J., Liang B. Q., Heymann K., Dathe L., Hanley K., Wirick S. and Jacobsen C. (2009) Carbon (1s) NEXAFS spectroscopy of biogeochemically relevant reference organic compounds. *Soil Sci. Soc. Am. J.* **73**, 1817–1830.

Solomon D., Lehmann J., Kinyangi J., Liang B. Q. and Schafer T. (2005) Carbon K-edge NEXAFS and FTIR-ATR spectroscopic investigation of organic carbon speciation in soils. *Soil Sci. Soc. Am. J.* **69**, 107–119.

Stevenson F. J. (1982) Organic forms of soil nitrogen. In *Nitrogen in Agricultural Soils* (ed. F. J. Stevenson). ASA, CSSA, SSSA, Madison, WI, pp. 67–122.

Theng B. (1979) *Formation and Properties of Clay-Polymer Complexes*. Elsevier Science Publishing Co., Amsterdam.

Tian S., Garcia-Rivera J., Yan B., Casadevall A. and Stark R. E. (2003) Unlocking the molecular structure of fungal melanin using $^{13}$C biosynthetic labeling and solid-state NMR. *Biochemistry (Wash.)* **42**, 8105–8109.

Toner B. M., Fakra S. C., Manganini S. J., Santelli C. M., Marcus M. A., Moffett J. W., Rouxel O., German C. R. and Edwards K. J. (2009) Preservation of iron(II) by carbon-rich matrices in a hydrothermal plume. *Nat. Geosci.* **2**, 197–201.

van Aken P. A. and Liebscher B. (2002) Quantification of ferrous/ferric ratios in minerals: new evaluation schemes of Fe L 2,3 electron energy-loss near-edge spectra. *Phys. Chem. Miner.* **29**, 188–200.

Wan J., Tyliszczak T. and Tokunaga T. K. (2007) Organic carbon distribution, speciation, and elemental correlations within soil microaggregates: applications of STXM and NEXAFS spectroscopy. *Geochim. Cosmochim. Acta* **71**, 5439–5449.

Warwick T., Ade H., Fakra S., Gilles M., Hitchcock A., Kilcoyne A. L. D., Shuh D. and Tyliszczak T. (2003) Further development of soft X-ray scanning microscopy with an elliptical undulator at the Advanced Light Source. *Synchrotron Radiat. News* **16**, LBNL-52407.

Watson H. R., Apperley D. C. and Dixon D. P. (2009) An efficient method for $^{15}$N-labeling of chitin in fungi. *Biomacromolecules* **10**.

Wershaw R. (2004) Evaluation of conceptual models of natural organic matter (humus) from a consideration of the chemical and biochemical processes of humification. U.S. Geological Survey, Reston, VA.

Zeglin L. H., Kluber L. A. and Myrold D. D. (2012) The importance of amino sugar turnover to C and N cycling in organic horizons of old-growth Douglas-fir forest soils colonized by ectomycorrhizal mats. In press: *Biogeochemistry*, http://dx.doi.org/10.1007/s10533-012-9746-8.

Zhong J., Frases S., Wang H., Casadevall A. and Stark R. E. (2008) Following fungal melanin biosynthesis with solid-state NMR: biopolymer molecular structures and possible connections to cell-wall polysaccharides. *Biochemistry (Wash.)* **47**, 4701–4710.

*Associate editor:* Jon Chorover